Membrane affinity difference between MinD monomer and dimer is not crucial for MinD gradient formation in *Bacillus subtilis*

Laura C. Bohorquez[1, 4], Henrik Strahl[2, #], Davide Marenduzzo[3], Martin J. Thiele[2, 5], Frank Bürmann[2, 6], Leendert W. Hamoen[1, #]

[1] The Bacterial Cell Biology, Swammerdam Institute for Life Sciences, University of Amsterdam, Amsterdam, The Netherlands.

[2] The Centre for Bacterial Cell Biology, Biosciences Institute, Newcastle University, Newcastle upon Tyne, United Kingdom.

[3] SUPA, School of Physics and Astronomy, The University of Edinburgh, Edinburgh, Scotland, United Kingdom.

[#] For correspondence: Henrik Strahl (h.strahl@ncl.ac.uk), Leendert Hamoen (l.w.hamoen@uva.nl)

[4] Present address: FIND, Geneva, Switzerland

[5] Present address: Carl Zeiss Meditec AG, Jena, Germany

[6] Present address: MRC Laboratory of Molecular Biology, Structural Studies Division, Cambridge, UK

Running title: Effect of MinD membrane affinity on gradient formation

ABSTRACT

Proteins can diffuse micrometers in seconds, yet bacterial cells are able to maintain stable protein gradients. The best studied bacterial protein gradient is the Min system of *Escherichia coli*. In rod-shaped bacteria the MinCD proteins prevent formation of minicells by inhibiting FtsZ polymerization close to the cell poles. In *E. coli* these proteins oscillate between cell poles within a minute, resulting in an increased MinCD concentration at the poles. This oscillation is caused by the interaction between MinD and the protein MinE, which form an ATP-driven reaction-diffusion system, whereby the ATPase MinD cycles between a monomeric cytosolic and a dimeric membrane attached states. *Bacillus subtilis* also has MinCD, but lacks MinE. In this case MinCD form a static gradient that requires the transmembrane protein MinJ, located at cell poles and cell division sites. A recent reaction-diffusion model was successful in recreating the MinD gradient in *B. subtilis*, assuming that MinD cycles between cytosol and membrane, like in *E. coli*. Here we show that the monomeric and dimeric states of *B. subtilis* MinD have comparable membrane affinities, that MinD interacts with MinJ as a dimer, and that MinJ is not required for membrane localization of MinD. Based on these new findings we tested different models, using kinetic Monte Carlo simulations, and found that a difference in diffusion rate between the monomer and dimer, rather than a difference in membrane affinity, is important for *B. subtilis* MinCD gradient formation.

42 **INTRODUCTION**

43

44 Bacterial cells are capable of positioning proteins at midcell and cell poles, and can form
45 protein gradients without the support of specific membrane compartments or guidance by
46 cytoskeleton elements, as found in eukaryotic cells. A well-known example is the formation
47 of a MinCD protein gradient along the cell axis of rod-shaped *E. coli* and *B. subtilis* cells.
48 These proteins ensure that cell division occurs at midcell and not close to cell poles (1). The
49 formation of these protein gradients is remarkable considering that the diffusion of proteins
50 in cells is in the order of µm square per second, whereas these bacteria are only a few µm in
51 length (2).

52 The Min system of *E. coli* is the best studied gradient system, and comprises the
53 membrane associated MinD and MinE proteins that form a reaction-diffusion couple (3-5),
54 resulting in a MinCD gradient that oscillates between cell poles in a matter of seconds (6, 7).
55 This system has been reconstructed on artificial membranes resulting in dynamic wave
56 patterns (8), and extensively simulated to understand the reaction parameters (e.g. (3-5, 9-
57 12)). *B. subtilis* also forms a MinD gradient that decreases in concentration from cell poles
58 and nascent cell division sites towards the middle of the cell. However, unlike *E. coli*, this
59 gradient does not oscillate (13-15). In this study, we investigated how the MinCD gradient is
60 formed in *B. subtilis*.

61 The core of the Min system consists of the protein couple MinC and MinD that
62 prevent aberrant polymerization of the key cell division protein FtsZ close to newly formed
63 septa or cell poles (15-17). MinC inhibits polymerization of FtsZ by direct protein-protein
64 interactions and needs to bind to the Walker A-type ATPase MinD for its recruitment to the
65 polar regions of the cell (18-21). Binding of ATP leads to MinD dimerization (22, 23), and

66 subsequent association with the cell membrane, whereby its C-terminal amphipathic helix
67 functions as membrane anchor (23, 24). MinC is recruited to the cell membrane by
68 association with MinD dimers (23, 25, 26). The *E. coli* Min system comprises a third protein,
69 the peripheral membrane protein MinE, that interacts with MinD, thereby displacing MinC
70 and stimulating the ATPase activity of MinD, which ultimately triggers the release of MinD
71 from the membrane (25, 27-30). The interaction with MinD causes a conformational change
72 in MinE that stimulates its membrane affinity (27). These reciprocal interactions of MinD
73 and MinE represent a natural reaction-diffusion system, resulting in the oscillation of MinCD
74 proteins between cell poles with a periodicity of approximately 50 seconds (6-8). Through
75 this oscillation, the average concentration of MinC is higher close to cell poles and lower at
76 midcell, thereby inhibiting polymerization of FtsZ close to cell poles and favoring Z-ring
77 formation at midcell (31).

78 The MinCD proteins of *E. coli* and *B. subtilis* are highly conserved. However, *B.*
79 *subtilis* does not encode a MinE homologue and instead requires the proteins DivIVA and
80 MinJ for the proper polar and septal localization of MinCD (32, 33). DivIVA is a general
81 scaffold protein conserved in Gram-positive bacteria that associates with strong negatively
82 curved membrane areas at the base of division septa, resulting in polarly located DivIVA
83 clusters after division is completed (34, 35). The integral membrane protein MinJ interacts
84 with DivIVA and shows the same localization pattern. MinJ also interacts with MinD, and
85 inactivation of MinJ eliminates a MinCD gradient, resulting in filamentous cells and minicell
86 formation due to uncontrolled activity of MinC (32, 33). Since DivIVA is recruited to midcell
87 in the early stages of septum synthesis when a strong concave membrane area is formed
88 (34), the Min proteins are already present when septum synthesis is ongoing, and their
89 primary activity it to inhibit Z-ring formation next to nascent division sites (15).

90 The ATP-driven cycle between membrane association and dissociation of MinD is
91 critical to the formation of the oscillating MinD gradient in *E. coli*. Mathematical modelling
92 has shown that such an ATP-driven reversible membrane attachment cycle can also explain
93 the formation of a MinD gradient in *B. subtilis* (36, 37). However, the C-terminal
94 amphipathic alpha helix of *B. subtilis* MinD has a much stronger affinity for the cell
95 membrane compared to its *E. coli* counterpart, and when fused to GFP can recruit this
96 protein to the cell membrane, which the *E. coli* MinD C-terminal membrane anchor is not
97 capable of (24). In fact, a MinD point mutant that prevents binding of ATP and maintains the
98 protein in its monomeric state is still recruited to the *B. subtilis* cell membrane (38). It is
99 therefore unclear whether dimerization-dependent changes in the membrane affinity of
100 MinD are crucial for the formation of a *B. subtilis* MinCD gradient.

101 In this study, we analyzed and manipulated the membrane affinity of *B. subtilis*
102 MinD, and combined *in vivo* experiments with *in silico* Monte Carlo simulations to assess the
103 role of membrane affinity in the formation of a MinCD gradient. The main difference
104 between our kinetic Monte Carlo model and previous mathematic models based on
105 reaction-diffusion equation is that our treatment is particle-based, rather than continuum
106 field-based, and naturally includes the effect of stochastic fluctuations, i.e. noise of the
107 system. The experiments demonstrated that, unlike in *E. coli*, a difference in membrane
108 affinity between MinD monomer and dimer is not critical for the creation of a MinCD
109 gradient. In addition, we examined how differences in MinD membrane affinity affect the
110 recruitment of MinC to the membrane, a process that is critical for the FtsZ-regulating
111 activity of the Min-system.

112

113 **RESULTS**

114

115 **Effect of dimerization on the localization of *B. subtilis* MinD**

116 We began by examining how much the membrane affinity of monomeric *B. subtilis* MinD
117 differs from the dimeric form by constructing MinD variants that are fixed in one of these
118 conformations. Dimerization of MinD and other members of the MinD/ParA protein family
119 requires binding of ATP. The conserved lysine in the Walker A-type ATPase domain, amino
120 acid position 16 in the protein (Fig. S1), forms hydrogen bonds with the phosphate groups of
121 the nucleotide, as revealed in the crystal structure of *Pyrococcus furiosus* MinD (39).
122 Exchanging this residue into an alanine (K16A, apo monomer) prevents ATP binding and
123 formation of dimers in several Walker motif-containing proteins, including *E. coli* MinD and
124 RecA, and *B. subtilis* ParA/Soj (40-42). The conserved glycine at position 12 makes contacts
125 with the γ-phosphate of ATP across the dimer interface (40). It has been shown that
126 changing this residue into a valine in *B. subtilis* ParA causes a steric clash in the active site
127 (G12V, ATP-bound monomer), thereby preventing dimerization while retaining ATP binding
128 (40, 42). These two monomer-forcing amino acid exchanges (K16A and G12V) were
129 introduced into *B. subtilis* MinD, which was fused at the N-terminus with GFP to follow its
130 localization in the cell. It has been shown that a GFP-MinD fusion retains its biological
131 activity (14), and the fusion protein was expressed at levels that resulted in normal sized
132 cells and the absence of minicells (Fig. 1A). To prevent possible localization artefacts due to
133 the weak dimerization characteristics of GFP (43), we used a monomeric GFP (mGFP)
134 variant. The different MinD fusion proteins were expressed from the ectopic *amyE* locus,
135 under control of the xylose-inducible *Pxyl* promoter (44), in a strain lacking wild type *minD*
136 (Δ*minD*), as well as in a strain lacking *minD* and *minC* (Δ*minCD*). Western blot analysis

137 showed that the different MinD-variants were stable and expressed at levels comparable to
138 that of wild type MinD (Fig. S2). Induction of mGFP-MinD with 0.1 % xylose reduced minicell
139 formation in a Δ*minD* background to wild type levels (from 14.7 % to 0.07 %, n > 300).
140 However, the mGFP-MinD-K16A and -G12V variants were unable to prevent formation of
141 minicells (11.2 % and 9.5 %, respectively, n > 600).

142 Fig. 1B shows the effect of the K16A exchange on mGFP-MinD localization. In line
143 with previous results (38), preventing the binding of ATP abolishes the mGFP-MinD
144 concentration gradient, which becomes clearer in longitudinal fluorescence intensity
145 profiles (Fig. 1, right panels). The fluorescence peaks visible at midcell are caused by the
146 presence of two septal cell membranes layers, as indicated by the fluorescence intensity
147 profiles of a wild type cell stained with the fluorescent membrane dye FM 5-95 (Fig. 1G).

148 The monomeric ATP binding G12V variant shows the same absence of a protein
149 gradient as the K16A variant (Fig. 1C). In contrast to *E. coli* MinD (29), both monomeric *B.*
150 *subtilis* MinD mutants still bind to the cell membrane. To measure the membrane
151 association *in vivo*, transverse fluorescence intensity profiles were collected (Fig. 1, middle
152 panels), and the membrane affinities were estimated based on the ratio between valley
153 (cytoplasmic) and peak (membrane) signals. This confirmed that the different monomeric
154 mutants have a comparable membrane affinity as wild type MinD (Fig. 1F). As controls we
155 used the fluorescence membrane dye FM5-95 and cells expressing cytosolic GFP (Fig. 1E).

156 It has been shown that exchanging a conserved aspartic acid residue in the ATPase
157 domains of *B. subtilis* ParA and *E. coli* MinD blocks ATP hydrolysis and traps the proteins in a
158 dimeric state (40, 42). When this aspartic acid residue, located at amino acid position 40 in
159 the *B. subtilis* MinD sequence (Fig. S1), was replaced by an alanine (D40A, ATP-bound dimer,
160 ATP hydrolysis deficient) in the mGFP-MinD fusion, expression of this variant in a Δ*minD*

161 strain resulted in highly filamentous cells with clusters of mGFP-MinD-D40A formed along
162 the membrane (Fig. 1D, left picture). Introduction of a *minC* deletion restored cell division
163 (Fig. 1D, right picture), indicating that the locked MinD dimer causes hyper activation of
164 MinC. Interestingly, in this Δ*minCD* background the clusters disappeared and mGFP-MinD-
165 D40A showed a clear polar and septal accumulation, although the polar and septal signal
166 intensities were approximately 60-70 % compared to that of wild type cells (Fig. S3B), and
167 the longitudinal protein gradient was clearly reduced (Fig. 1D and S3A). Quantification of the
168 membrane affinity showed that the membrane affinity of the D40A variant is only slightly
169 higher compared to the monomeric mutants (Fig. 1F).
170
171 **Localization of trapped MinD dimer depends on MinJ**
172 The polar and septal localization of the D40A trapped dimer-variant of MinD presumably
173 relies on the interaction with MinJ. It has been reported that the absence of MinJ results in
174 detachment of MinD from the membrane (32, 37). However, when we introduced the Δ*minJ*
175 in our Δ*minCD* deletion strain background we found that all MinD-GFP variants remained
176 attached to the membrane, and the septal and polar localization of wild type and the
177 trapped dimer MinD disappeared (Fig. 2). These results show that, while MinJ is not
178 required for membrane attachment of MinD *per se,* it is required for polar and septal
179 localization of MinD through interactions specifically with the dimeric form of MinD.
180
181 **Recruitment of MinC by the different MinD mutants**
182 Several biochemical studies with different bacterial species, including *B. subtilis*, have shown
183 that MinC and MinD dimers can assemble into long polymers (45-48). However, the
184 assembly of large MinCD multimers has not been observed *in vivo*, and a genetic study

185 indicated that the formation of such polymers are not necessary for the function of the Min
186 system in *E. coli* (49). The D40A MinD variant showed a clustered membrane localization
187 pattern that resolved into a smooth membrane pattern when *minC* was deleted (Fig. 1D).
188 This change in localization pattern might be related to the formation of higher-order MinCD
189 assemblies. To confirm this, we introduced an active mCherry-MinC fusion to see whether
190 mGFP-MinD and mCherry-MinC would colocalize when the former is fixed in a dimeric state.
191 First, we examined the localization of MinC in the presence of monomeric K16A and G12V
192 MinD variants. As shown in Fig. 3B and C, the mCherry-MinC signal was dispersed
193 throughout the cytosol in these strains, indicating a lack of interaction with monomeric
194 MinD variants, in line with a previous report (38). In case of the mGFP-MinD-D40A variant,
195 the mCherry-MinC expression was only induced for 1 h to prevent excessive filamentation.
196 As shown in Fig. 3D, the mCherry-MinC signal showed foci along the membrane that often
197 colocalized with mGFP-MinD-D40A foci, confirming that MinD dimerization is crucial for
198 MinC interaction, and that both proteins can indeed form large assemblies in the cell,
199 presumably in the form of MinCD copolymers.

200 The colocalization of the MinD-D40A and MinC fluorescent fusion proteins enabled
201 us to investigate whether MinD dimerization is sufficient for MinC activity or whether
202 localization at the cell membrane is also required. To test this, the membrane binding
203 capacity of MinD was impaired by replacing isoleucine 260, located in the C-terminal
204 membrane targeting amphipathic alpha helix, with a glutamate residue (Fig. 3E) (50). Next,
205 we introduced this mutation in the mGFP-MinD-D40A mutant to create a trapped MinD
206 dimer that was no longer able to bind to the membrane. Expression of this cytosolic MinD
207 variant did not result in cell filamentation (Fig. 3F), indicating that interaction with MinD
208 dimers alone is not sufficient to inhibit FtsZ polymerization. Rather, MinC needs to be

209 localized and enriched to the membrane surface to be effective, which is not surprising
210 since Z-ring formation occurs at the membrane periphery.
211
212 **Weak membrane interaction is important for MinD gradient formation**
213 The absence of a clear difference in membrane affinity between monomeric and dimeric
214 MinD raised the question whether a reversible membrane binding is important for the
215 formation a protein gradient. To examine this, we tried to increase the membrane affinity of
216 MinD by adding an extra copy of its C-terminal membrane targeting amphipathic helix. The
217 extra amphipathic helix was connected to the original helix by a short 11 amino acid long
218 flexible linker (Fig. 4A). First, we tested whether such tandem amphipathic helix (2xAH)
219 increases the membrane affinity by fusing it to mGFP. As shown in Fig. 4, fusion of this
220 tandem helix to mGFP increased the membrane association of the latter considerably when
221 compared to a single MinD amphipathic helix.
222 Next, we replaced the membrane targeting amphipathic helix of mGFP-MinD by the
223 tandem amphipathic helix. Western blot analysis showed that this new C-terminus did not
224 affect the protein levels to a significant degree (Fig. S2). As shown in Fig. 5B and D, the
225 tandem helix notably increased the fluorescent membrane signal all along the cell
226 membrane, thereby reducing the longitudinal fluorescence gradients.
227 To confirm that the tandem amphipathic helix increased the membrane affinity of
228 MinD, we tested its sensitivity to membrane depolarization. Previously, it has been shown
229 that binding of the MinD amphipathic helix to the cell membrane requires the presence of
230 the membrane potential (50). Dissipation of the proton motive force by the specific proton-
231 ionophore carbonyl cyanide m-chlorophenylhydrazone (CCCP) did not affect the membrane
232 localization of the tandem amphipathic helix fusion, whereas CCCP quickly disturbed the

233 membrane attachment of wild type MinD (Fig. S5).

234 We also tested what happens with the MinD gradient when its membrane affinity is
235 reduced. For this, the well-studied membrane binding amphipathic helix 2 from the
236 Hepatitis C virus protein NS4B was chosen (51, 52), which is hardly able to attach mGFP to
237 the cell membrane (Fig. 4). Replacing the wild type membrane targeting helix of MinD by
238 the weak NS4B amphipathic helix reduced the membrane association of mGFP-MinD (Fig.
239 5D), as well as its septal and polar localization (Fig. 5C and Fig. S4). Interestingly, this mutant
240 still displayed a longitudinal protein gradient. Together these data suggests that a reversible
241 membrane association is important for the formation of a MinD gradient along the cell axis.

242

243 **Effect of MinD membrane affinity on MinC recruitment and activity**

244 The results shown in Fig. 3 indicated that the attachment of the MinD dimer to the
245 membrane is essential for the activity of MinC. When this attachment was strengthened by
246 using the tandem amphipathic helix, the respective strain regularly featured additional
247 septa resulting in minicells (Fig. 5B, red arrows), although the frequency was lower
248 compared to a Δ*minD* mutant (Fig. 6A). The strain also exhibited an elongated cell
249 phenotype that was comparable to that of the *minD* deletion strain (Fig. 6B). As shown in
250 Fig. 7B, the mGFP-MinD(2xAH) variant is capable of recruiting mCherry-MinC along the
251 whole cell membrane, which likely explains the elongated cell phenotype.

252 Weakening the membrane affinity of mGFP-MinD, by replacing the wild type
253 amphipathic helix with the NS4B amphipathic helix, also resulted in occasional minicell
254 formation, but again not as numerous as in a *minD* deletion strain (Fig. 6A). The cell length
255 distribution of the strain expressing the mGFP-MinD(NS4B-AH) variant was closer the wild
256 type strain (Fig. 6B). When mCherry-MinC was co-expressed in this strain background, also

257 the MinC fusion protein showed a clear fluorescent gradient along the cell axis (Fig. 7C).
258 Thus, a reversible association of MinD with the cell membrane seems to be critical to
259 prevent misplacing the FtsZ inhibiting activity of MinC along the cell axis. Both the mGFP-
260 MinD(2xAH) and mGFP-MinD(NS4B-AH) variants were, at least partially, able to prevent
261 minicell formation, presumably because they are still recruited to cell poles and cell division
262 sites through interaction with MinJ.
263
264 **Membrane gradient formation in kinetic Monte Carlo simulations**
265 The different experiments indicated that the formation of a MinCD gradient requires the
266 dynamic switching between monomer and dimer states of MinD (Fig. 1), and a reversible
267 MinD membrane interaction (Fig. 5). So far, *in silico* simulations of the *B. subtilis* Min
268 gradient have assumed a strong difference in membrane interaction between the
269 monomeric and dimeric state of MinD, which is based on properties of the *E. coli* Min
270 system (36, 37). However, our data suggests that for *B. subtilis* these affinities do not differ
271 much (Fig. 1). To investigate more closely whether a difference in membrane affinity
272 between monomer and dimer is required for the formation of a MinD gradient in *B. subtilis*,
273 we resorted to kinetic Monte Carlo simulations (see Methods for more details). The Monte
274 Carlo algorithm attempts to move one molecule at a time by a small amount in a three-
275 dimensional space. The new interaction energy experienced by the particle is then
276 calculated and compared with its old energy, and the move is subsequently accepted or
277 rejected according to the standard Metropolis test (53, 54). This procedure is used to guide
278 the system to the correct Boltzmann distribution in equilibrium. It has been shown that this
279 Monte Carlo dynamics corresponds well with Brownian or molecular dynamics (55, 56), and
280 can be used to examine mechanisms underlying spatiotemporal protein gradients in cells

281 (34), provided that the moves are small enough and that the acceptance probability remains
282 high (55).

283 MinD monomers were presented as spheres (hydrodynamic radius 2.5 nm) that
284 diffuse within and along a spherocylindrical cell geometry. The following rules were
285 implemented: (i) Diffusion along the membrane is 10-fold slower that through the
286 cytoplasm, and (ii) the dimer, due to its larger diameter, diffuses 2-fold slower compared to
287 the monomer in both environments, emanating from Stokes-Einstein law and a
288 hydrodynamic radius for the dimer which is double that of the monomer. (iii) Based on the
289 data from Fig. 3, we started out with a 10 % stronger membrane affinity for the dimer. (iv)
290 The membrane dwell time of monomers and dimers is 0.01 - 0.5 sec and during the
291 simulations approximately 70 % of MinD molecules reside at the membrane, approaching
292 the valley to peak values observed experimentally (Fig. 1F). (v) Dimerization and
293 monomerization are modelled as chemical reactions between a monomer and a dimer
294 state. Baseline rates are set such that the two states are in a 1:1 ratio, based on the
295 longitudinal fluorescence intensity profile in Fig. 1A, and the assumption that dimers are
296 located at the polar regions and monomers along the lateral wall. In our baseline model,
297 dimerization at the pole, membrane and in the cytoplasm is equally likely, and is modelled
298 in a simple way as a reaction turning a monomeric to a dimeric MinD at constant rate. (vi)
299 The transition from dimer to monomer, stimulated by ATP hydrolysis, occurs stochastically
300 with a half-life of approximately 1/sec, which is based on information from *E. coli* MinD (5).
301 (vii) MinD dimers that come in close proximity of MinJ, represented as the surface area at
302 the polar caps, will remain attached to MinJ for some time, so that approximately 25 % of
303 MinD dimers is associated with MinJ, reminiscent of the septal localization of the D40A
304 variant (Fig. S3). We simulated 10^7 time steps, corresponding to about 100 s real time,

305 when the system is in steady state. Simulation details are described in the material and
306 methods, and a full list of parameters and their typical values considered in simulations is
307 presented in Table S1.

308 When we applied these rules and ran the simulation, a strong accumulation of MinD
309 at the poles was observed, but no gradient (Fig. 8A). In this simulation, the chance that
310 MinD can form a dimer is the same for monomers in the cytoplasm and those that are
311 attached to the membrane. However, it is likely that dimer formation in the latter situation
312 is more likely since monomers attached to the membrane by their C-terminal amphipathic
313 helix will diffuse slower and therefore spend more time in close proximity and, importantly,
314 they have the same spatial orientation, which will facilitate dimerization. However, when we
315 repeated the simulation, and implemented that membrane attached monomers have a 2-
316 fold higher chance of forming dimers than monomers in the cytoplasm, the localization
317 pattern did not change (Fig. 8B).

318 Since it seems that MinJ interacts with the dimer form of MinD (Fig. 2), there is the
319 possibility that MinJ actually stimulates MinD dimerization. Interestingly, when this property
320 was added to the simulation, a clear MinD gradient emerged along the cell length, together
321 with a strong polar localization signal (Fig. 8C), a pattern that is in good agreement with the
322 longitudinal fluorescence intensity profiles observed *in vivo* (Fig. 1A). This pattern did not
323 change when we included the condition that only membrane attached dimers are able to
324 revert to monomers (Fig. 8D, E), in agreement with a recent report showing that the ATPase
325 activity of MinD depends on its interaction with lipid membranes (57). In the simulation of
326 Fig. 8E, we repeated the simulation of Fig. 8D, but increased the ATPase activity, i.e. dimer-
327 to-monomer transition 10-fold. This enhances MinD gradient formation.

328 When we performed the simulation of Fig. 8C but now with the assumption that

329 MinJ only stimulates dimerization and does not bind MinD dimers, a MinD gradient is still
330 formed, although the strong accumulation at the polar caps was abolished (Fig. 8F).
331 Subsequently, we repeated the simulation of Fig. 8C under conditions whereby there was no
332 difference in the diffusion rate of monomer and dimer (Fig. 8G). In this case the MinD
333 gradient was completely lost, showing that the differential diffusion of monomers and
334 dimers is necessary to create a steady-state gradient.

335 Next, we tested the role of the membrane affinity in gradient formation. First, the
336 simulation of Fig. 8C was repeated without a difference between the membrane affinity of
337 the MinD monomer and dimer (Fig. 8H). Interestingly, under these conditions the MinD
338 protein gradient is still being formed. When we repeated the simulation of Fig. 8C and kept
339 the 10 % difference in membrane affinity between MinD monomer and dimer, but made
340 their membrane affinities stronger, the gradient was reduced (Fig. 8I), in good agreement
341 with our *in vivo* observation with a MinD variant containing a tandem membrane anchor
342 (Fig. 5B). We then tested what happens when the simulation of Fig. 8C was repeated with a
343 weaker membrane affinity of MinD. As shown in Fig. 8J, a clear gradient is formed, again in
344 line with what was found when the membrane targeting amphipathic helix of MinD was
345 replaced with the weaker amphipathic helix 2 from Hepatitis C virus protein NS4B (Fig. 5C).

346 It has been shown that purified *E. coli* MinD can form large polymers in the presence
347 of ATP (58), and when bound to membranes can stimulate multimerization (59).
348 Multimerization might further increase the diffusion difference between monomer and
349 dimer, thus contributing to the formation of a protein gradient. Multimerization is
350 challenging to model in our simulation setup, but as an approximation we tested what
351 happens when MinD dimers can form tetramers. We ran a simulation whereby the baseline
352 rates of dimer to tetramer and tetramer to dimer formations were equal. However this did

353 not lead to a dramatic change in MinD gradient (Fig. 8K). In conclusion, our kinetic Monte
354 Carlo simulations suggests that the formation of a MinD gradient requires: (i) a reversible
355 and not too strong interaction of MinD with the membrane, (ii) a clear difference between
356 the diffusion rates of monomer and dimer, (iii) an ATPase driven dimer-monomer cycle, and
357 (iv) the stimulation of dimerization at the cell poles and division sites. Importantly, a
358 difference in membrane affinity between monomer and dimer is not required.

359 **DISCUSSION**

360

361 **Protein gradients in bacteria**

362 Due to their small size, proteins diffuse rapidly throughout bacterial cells, in a matter of
363 seconds, yet stable protein gradients can be found in a large variety of bacteria. What these
364 systems have in common, including the MinD gradient, is a locally reduced diffusion rate of
365 the proteins involved, which allows stable protein concentration gradients to form. The
366 viscosity of the cell membrane is roughly 100 times larger compared to the cytoplasm (60,
367 61), and the Min system uses attachment to the cell membrane to slow down diffusion.
368 Another approach to reduce diffusion is to bind to DNA, which occurs in the ParABS system
369 involved in chromosome segregation in the asymmetric bacterium *Caulobacter crescentus*
370 (62). This system consists of the ParA ATPase, which belongs to the same ATPase family as
371 MinD (63) and ParB that binds to *parS* DNA binding sites. The ParA dimers associate with
372 DNA nonspecifically whereby ParB stimulates ATP hydrolysis of ParA dimers, resulting in the
373 dissociation from DNA. The localized dissociation and subsequent increased diffusion rate
374 results in a ParA concentration gradient away from the *parS* locus (64). The cyanobacterium
375 *Synechococcus elongatus* uses the ParA-like protein McdA to position carboxysomes along
376 the longitudinal axis. In this system, the protein McdB, which interacts with carboxysomes,
377 stimulates McdA ATPase activity and its release from DNA, resulting in an oscillation of
378 McdA over the nucleoid (65). Recently it was described that *Staphylococcus aureus* trigger
379 factor (TF) forms a gradient by interacting with the cell division protein FtsK, resulting in an
380 increased TF concentration towards the septal region (66). How TF reduces its diffusion in *S.*
381 *aureus* cells is still unclear but might be a consequence of the fact that the chaperone
382 directly interacts with ribosomes (67), which diffuse much slower due to their size and

383 association with mRNA and nascent polypeptide chains.

384

385 **Previous MinD gradient modelling studies**

386 As mentioned in the introduction, there are many mathematical models describing the
387 oscillating MinD gradient of *E. coli* but so far only two mathematical models focused on the
388 MinD gradient of *B. subtilis* (36, 37). Both models make use of the reversible interaction of
389 MinD with the cell membrane. The first study, almost 20 years ago, modelled the
390 localization of DivIVA and MinD by a reaction-diffusion system in one spatial dimension (36).
391 At that time neither MinJ nor the localization mechanism of DivIVA were known. In this
392 early study both MinD and DivIVA were assumed to cycle between the membrane and the
393 cytosol, and the membrane attachment of DivIVA would depend on MinD, whereas the
394 membrane attachment of the latter would be stabilized at the cell poles by DivIVA.
395 However, we now know that DivIVA binds to the membrane by itself, and there is no
396 interaction between MinD and DivIVA (34).

397 The ATPase stimulated monomer-dimer cycle of MinD was not included in this early
398 model, but it was used in a recent study that employed a minimal reaction-diffusion system
399 in three-dimensional cellular space (37). In this model *B. subtilis* MinD cycles between the
400 cell membrane and cytosol, whereby the membrane detached MinD is in the ADP-bound
401 state and can only rebind after exchanging ADP for ATP, like in *E. coli*. By assuming that the
402 membrane recruitment rate is higher at the poles and septa due to the presence of MinJ or
403 due to a kinetic increase of diffusional impacts with the membrane due to the curved
404 geometry at poles, a steep MinD gradient could be simulated (37).

405

406 **New data on MinD localization**

407 Here, we have shown that monomeric MinD, both in its ATP-bound and unbound state, has
408 a membrane affinity that is comparable to that of the dimeric form of MinD, which is clearly
409 different from *E. coli* MinD that requires dimerization for membrane association. In fact, it
410 has been shown that the C-terminal membrane targeting amphipathic helix of *E. coli* is
411 considerably weaker than that of *B. subtilis* MinD, and that stable membrane binding is only
412 possible when a dimer is formed so that there are two membrane targeting domains (24).
413 Our findings are in good agreement with a recent report showing a strong membrane
414 affinity for purified monomeric *B. subtilis* MinD for liposomes, independent of the presence
415 of ATP (57).

416 We have also shown that MinJ is not required for the membrane recruitment of
417 MinD (Fig. 2). We have no explanation for the differences between our findings and that of
418 the previous studies in which it has been shown that MinJ is needed for the membrane
419 localization of MinD (32, 37). However, since the membrane-targeting amphipathic alpha
420 helix of *B. subtilis* MinD is by itself sufficient to recruit GFP to the cell membrane, even in *E.*
421 *coli*, which does not contain a MinJ homologue (24, 50), it is difficult to envision how the
422 absence of MinJ would bring MinD to the cytosol.

423 In another study, it has been suggested that the C-terminal amphipathic helix of
424 MinD by itself is sufficient to recruit GFP to cell division sites, even in the absence of either
425 MinJ or DivIVA (68). However, as indicated in Fig. 1, the presence of two perpendicular-
426 observed membranes that are formed during septum synthesis gives a higher fluorescence
427 membrane signal, which might have been mistakenly interpreted as septal localization. In
428 addition, in our hands a GFP fusion with the C-terminal amphipathic helix of *B. subtilis* MinD
429 shows a clear fluorescence membrane stain but no accumulation at division sites (Fig. 4B).
430

431 **Kinetic Monte Carlo model**

432 Our *in vivo* findings warranted a new mathematical model to study the formation of the *B.*
433 *subtilis* MinD gradient (see Methods for more details). The kinetic Monte Carlo model
434 showed that a membrane attachment-detachment cycle is not required to form a protein
435 gradient, but that a dynamic ATP-driven cycle between monomer and dimer is crucial,
436 coupled to the differences in diffusion rates. We have shown that the MinD dimer
437 associates with MinJ, but this by itself, even when the interaction was reversible, was not
438 enough to create a gradient. We ascribe this to the fact that both monomers and dimers
439 bind to the membrane with small difference in affinities in our model, whereas in (37) the
440 monomer state is not membrane-associated. To establish a gradient in our simulations, we
441 needed to include the requirement that MinJ stimulates and/or stabilizes MinD
442 dimerization, but this MinJ activity remains speculative. It should be stressed that MinJ is
443 not crucial for MinD dimerization, since a *minJ* mutant shows a strong filamentous
444 phenotype that can be suppressed by a *minC* deletion, indicating that MinD dimerization,
445 required for MinC activity, also occurs in the absence of MinJ.

446 Although a difference in membrane affinity between monomer and dimer is not
447 necessary to establish a gradient, the modelling shows that a transient and reversible
448 membrane binding of MinD is necessary. This was also confirmed by the reduced formation
449 of a gradient when the membrane affinity of MinD was increased by using a tandem C-
450 terminal amphipathic helix (Fig. 5B). This can be explained by considering the emergent
451 length scale over which the gradient develops. As in reaction-diffusion models for
452 morphogenesis, this length scale is given by the square root of a diffusion coefficient over a
453 reaction rate. Our simulations suggest that a possible formula is given by $l \sim \sqrt{\frac{D_m - D_d}{k_m}}$, with

454 D_d and D_m the dimer and monomer diffusion (the relevant rate is that on the membrane),
455 and k_m the rate of conversion between dimers and monomers. Increasing the interaction
456 with the membrane leads to a decrease in diffusivity, and concomitantly a reduction in the
457 length scale over which the gradient can be observed.

458 In our modelling, MinJ is simply represented by the polar cap area. FRAP studies
459 have shown that the recruitment of MinJ to cell poles and division sites is quite dynamic
460 with a fluorescence recovery rate close to a minute (37). However, the fluorescence
461 recovery rate of MinD is approximate 8-fold higher (37). Because of this large difference in
462 diffusion rates, we have ignored the diffusion of MinJ in our modelling. We do not foresee
463 different results if we were to include MinJ diffusion in our Monte Carlo simulations,
464 provided that in steady state MinJ is on average localized at the poles.

465 Another aspect that we have only partially addressed in the simulations is MinD
466 polymerization. It has been shown that purified *E. coli* MinD can form large polymers in the
467 presence of ATP (58), and, when bound to membranes, can stimulate multimerization (59).
468 In our simulations we tested the effect of MinD tetramerization, however, this did not
469 improve MinD gradient formation (Fig. 8K). It should be mentioned that formation of large
470 polymers was not found with purified *B. subtilis* MinD (48). Moreover, FRAP experiments
471 with *B. subtilis* shows a fluorescence recover rate of seconds for MinD at division sites (37),
472 suggesting that if such polymers exist, they are not very stable. Thus, it remains to be seen
473 whether MinD multimerization is relevant in *B. subtilis* cells.

474 In conclusion, we have shown here that a dynamic cyclic change in membrane
475 affinity of MinD is not required for the formation of a concentration gradient in the cell.
476 Instead, our modelling suggests that stimulation of MinD-dimerization at cell poles and cell
477 division sites is needed. It will be interesting to see whether future experiments proves this

suggestion right or wrong.

479 **MATERIAL AND METHODS**

480

481 **Bacterial strains, growth conditions and media**

482 Luria-Bertani (LB) agar was used for the routine selection and maintenance of both *B.*
483 *subtilis* and *E. coli* strains. For *B. subtilis*, cells were grown in LB medium or Spizizen minimal
484 salt medium supplemented with 0.05 % yeast extract (SMMY). SMMY consists of 2 g/l
485 $(NH_4)_2SO_4$, 14 g/l K_2HPO_4, 6 g/l KH_2PO_4, 1 g/l sodium citrate, 2 g/l $MgSO_4$, 5 g/l fructose, 2 g/l
486 tryptophan, 0.2 g/l casamino acids and 2.2 g/l ammonium ferric citrate. All strains were
487 grown at 37 °C. The supplements were added as required: 100 µg/ml ampicillin, 5 µg/ml
488 chloramphenicol, 5 µg/ml kanamycin, 100 µg/ml spectinomycin, 10 µg/ml tetracycline and 1
489 µg/ml erythromycin. The *B. subtilis* strains used are listed in Table S2. The mutant strains
490 kindly provided by other labs were transformed into our laboratory strain to ensure that all
491 strains were isogenic.

492

493 **Strain constructions**

494 Molecular cloning, PCR and transformations were carried out by standard techniques.
495 Plasmids and oligonucleotides used in this study are listed in Table S3 and S4, respectively.
496 The *minC*, *minD*, *minCD* and *minJ* gene deletions were introduced from existing strains listed
497 in Table S2 by standard natural transformation (69). The *aprE*-integration vector containing
498 mCherry under an IPTG-inducible promoter (P*spac*) was constructed as follows. The
499 spectinomycin marker of pAPNC213 (70) was replaced with a chloramphenicol resistance
500 cassette (*cat*) using In-Fusion cloning (Clonetech). For this aim pAPNC123 was PCR-linearized
501 with oligonucleotide pair HS05/HS06 and the *cat* cassette was amplified from pSG2 (71)
502 with oligonucleotide pair HS07/HS08. These PCR products were fused together with In-

503 Fusion cloning, resulting in pAPNC*cat,* this plasmid was verified by sequencing. Next, the
504 mCherry encoding gene was amplified using oligonucleotide pair HS437/HS438 and plasmid
505 template pSS153 (72) as template. SalI and BamHI restriction sites were inserted into the
506 primers. The mCherry PCR product and the pAPNC*cat* were digested with SalI and BamHI
507 and ligated. The resulting plasmid was verified by sequencing and named pHJS112.

508 The IPTG-inducible mCherry-*minC* fusion was constructed as follows. A PCR fragment
509 containing *minC* was amplified with oligonucleotide pair LB1/LB2 and genomic DNA of the
510 wild type strain 168 as template. BamHI and EcoRI restriction sites were inserted into the
511 primers. The PCR product and the *aprE*-integration vector pHJS112 were digested with
512 BamHI and EcoRI restriction enzymes and ligated. The resulting plasmid pLB11 was verified
513 by sequencing and transformed into *B. subtilis* competent cells, resulting in strain LB31. The
514 *aprE* integration was verified by PCR, amplifying the genomic DNA with oligonucleotide pair
515 HS508/HS509 and sequencing.

516 The *amyE*-integration vector pSG1730 containing GFP fused to *minD* under a xylose-
517 inducible promoter (13) was used to exchange the *minD* residue glycine 12 to valine (G12V)
518 and aspartic acid 40 to alanine (D40A), by incorporation of the corresponding mutation
519 using the QuickChange site-directed mutagenesis reaction (Stratagene) and the
520 oligonucleotide pairs HS320/HS321 and HS322/HS323, respectively. The resulting plasmids
521 were verified by sequencing and named pHJS115 and pHJS116, respectively. The plasmid
522 pHJS113 containing GFP fused to *B. subtilis minD* coding sequence with the lysine 16 to
523 alanine (K16A) exchange under a xylose-inducible promoter was reported previously (50).

524 Plasmid pSG1729 (44), containing GFP under a xylose-inducible promoter, was used
525 to generate a construct with GFP fused to the native *minD* membrane targeting amphipathic
526 helix (KGMMAKIKSFFG). This domain was amplified from *B. subtilis* wild type strain 168 with

527 oligonucleotide pair FB136/FB149. EcoRI and BamHI restriction sites were inserted into the
528 primers. The PCR product and the plasmid pSG1729 were digested with EcoRI and BamHI
529 restriction enzymes and ligated. The new plasmid was verified by sequencing and named
530 pHJS117. Plasmid pHJS117 was used to generate a construct with GFP fused to two *minD*
531 amphipathic helices in tandem with a short linker of glycines in between (2xAH). This
532 tandem membrane targeting sequence was created by amplification with oligonucleotides
533 FB138/FB149 and pHJS117 as template. The primer FB138 carries a long overhang that
534 generates an extra MinD membrane targeting amphipathic helix fused to the existing
535 membrane targeting domain (KGMMAKIKSFFGVRS**GG**VLEEQNKGMMAKIKSFFG). EcoRI and
536 BamHI restriction sites were inserted into the primers. The PCR product and the plasmid
537 pSG1729 were digested with *Eco*RI and *Bam*HI restriction enzymes and ligated. The new
538 plasmid was verified by sequencing and named pHJS119.

539 Another construct with GFP fused to the NS4B amphipathic helix 2 from Hepatitis C
540 virus (NS4B-AH) was generated as follows. Plasmid pSG1729 was amplified with
541 oligonucleotides FB141/FB149. The primer FB141 carries a long overhang that generates the
542 NS4B-AH anchor (TVTQLLRRLHQWI). EcoRI and BamHI restriction sites were inserted into
543 the primers. The PCR product and the plasmid pSG1729 were digested with EcoRI and
544 BamHI restriction enzymes and ligated. The new plasmid was verified by sequencing and
545 named pHJS121.

546 We constructed two different *amyE*-integration plasmids with GFP fused to *minD*
547 with different membrane targeting sequences. The native *minD* amphipathic helix was
548 either replaced with two *minD* amphipathic helices in tandem with a short linker of glycines
549 in between (MinD2xAH) or with the Hepatitis C virus NS4B amphipathic helix 2 (MinDNS4B-
550 AH). The *minD* gene was amplified from the *B. subtilis* genome (strain 168) with

551 oligonucleotides pairs FB135/FB138 and FB135/FB141, respectively. BamHI and EcoRI
552 restriction sites were inserted into the primers. The primers FB138 and FB141 carry a long
553 overhang that generates the 2xAH and the NS4B-AH, respectively. The digested PCR
554 fragments were ligated with BamHI/EcoRI-linearized pSG1729, containing GFP under a
555 xylose-inducible promoter. The new plasmids were verified by sequencing and named
556 pHJS123 and pHJS125, respectively.

557 Plasmids pSG1730, pHJS113, pHJS115, pHJS116, pHJS123 and pHJS125 were used as
558 template for the QuickChange site-directed mutagenesis reaction (Stratagene) with
559 oligonucleotide pair HS410/HS411 to introduce the A206K exchange in the GFP coding
560 sequence to reduce protein dimerization (mGFP). The resulting plasmids were verified by
561 sequencing and named pLB21, pLB22, pLB23, pLB24, pLB49 and pLB50 respectively.
562 Plasmids pLB21 and pLB24 were used to further exchange the *minD* isoleucine 260 to
563 glutamic acid (I260E) by QuickChange site-directed mutagenesis reaction (Stratagene) with
564 oligonucleotide pair HS205/HS206. The resulting plasmids were verified by sequencing and
565 named pLB71 and pLB72, respectively. These constructs were integrated at the *amyE* locus
566 in different genetic backgrounds.

567

568 **Western blot analysis**

569 To detect the cellular levels of the different GFP-MinD variants the strains were induced
570 with 0.1 % xylose for three doublings. 2 ml of cultures, with comparable ODs were
571 centrifuged and the cell pellets flash frozen in liquid nitrogen. The pellets were then
572 resuspended in 200 µl of buffer containing 10 mM Tris-Hcl pH 8, 100 mM NaCl and 1 %
573 TritonX-100. The cells were lysed with 100 µg/ml lysozyme during 15 min incubation at
574 room temperature. Cell debris were spun down (20 min Eppendorf centrifuge, 14000 rpm,

575 4°C) and 10 µl of samples were loaded onto a 10 % SDS-PAGE followed by separation by
576 electrophoresis at 150 V for 60 min. The proteins were then transferred to a PVDF
577 membrane (Thermo Scientific) with transfer buffer (14.4 g/l glycine, 3 g/l Tris base and 15 %
578 methanol) using mini-wet electroblotting system (Bio-Rad) at 55 V for 130 min. The
579 transferred membrane was then blocked in blocking buffer (1 % skimmed milk powder in
580 TBST buffer 50 mM Tris, 150 mM NaCl and 0.05 % Tween-20) overnight and rinsed twice for
581 5 min in TBST. The proteins were probed with a 1:2000 dilution of rabbit anti-GFP primary
582 antibody (Invitrogen) in 10 ml TBST incubated 1 h, the membrane was washed 3x in TBST
583 and incubated in a 1:20 000 dilution of secondary antibody goat anti rabbit IR dye (Li-cor
584 Biosciences) in 10 ml TBST during 1 h. The immunoblot was developed by using an Odyssey®
585 imaging system (Li-cor Biosciences).
586
587 **Microscopy**
588 Microscopy was performed on an inverted fluorescence Nikon Eclipse Ti microscope
589 equipped with a CFI Plan Apochromat DM 100x oil objective, an Intensilight HG 130bW lamp
590 and C11440-22CU Hamamatsu ORCA camera. Images were analysed using ImageJ v.1.48d5
591 (National Institutes of Health) software and the plugin ObjectJ (73). To measure the
592 transverse fluorescence intensity profiles (FIP), line-scans perpendicular to the cell axis were
593 marked. The polar gradient areas, marked in red in figures, were manually assigned by
594 means of visual inspection of the fluorescence gradient of the FIPs. The membrane affinity
595 was estimated as the ratio valley/peaks of the transverse FIP, using an average of at least 30
596 cells per data set. When appropriate, data was analyzed with t-tests (p-values) using
597 GraphPad Prism for Mac, GraphPad Software.
598 For microscopy, cells were grown to exponential phase by diluting 1:100 a starter

599 culture grown overnight in liquid medium (SMMY) into fresh medium, and allowing at least
600 three doublings before mounting on microscopy slides covered with a thin film of 1 %
601 agarose. 0.1 % xylose and 0.01 mM IPTG were used for the induction since these
602 concentrations complemented a Δ*minCD* deletion strain, preventing minicell formation.
603 Membranes were stained with the fluorescent membrane dye FM-95 (0.5 µg/ml final
604 concentration), incubated for 5 min prior to mounting onto microscope slides covered with
605 a thin film of 1 % agarose. Dissipation of the proton motive force (pmf) was carried out by
606 the addition of 100 µM carbonyl cyanide m-chlorophenylhydrazone (CCCP) for 10 min. CCCP
607 was dissolved in DMSO (0.1 % final concentration of DMSO). As control, cells were
608 incubated with 0.1 % DMSO.
609
610 **Kinetic Monte Carlo simulations**
611 To model the formation of a steady state gradient in *B. subtilis* wild-type cells and mutants,
612 kinetic Monte Carlo simulation were performed. Kinetic Monte Carlo is a stochastic
613 algorithm which is known to be equivalent to molecular dynamics for sufficiently small local
614 moves (55, 56). The system simulated consisted in a collection of 1000 MinD proteins
615 enclosed inside a spherocylinder, with cap diameter $2R_{cyl}$ and total height h_{cyl} (we chose
616 an aspect ratio $\frac{h_{cyl}}{2R_{cyl}}$ =4, sizes 80 by 20 in simulation units) modelling a *B. subtilis* cell. MinD
617 proteins can be in one of two states, either monomeric (M) or dimeric (D). The M and D
618 states have both affinities for the membrane (the surface of the spherocylinder). To model
619 this, we introduce an attractive potential, a square well with range 1 and strength ϵ_M and ϵ_D
620 for the M and D state respectively. Given our experimental results that the dimer is only
621 weakly stickier than the monomer, we ran our simulations with $\epsilon_D = 1.1\,\epsilon_M$, and ϵ_M=1 k_BT.

622 Additionally, the D state, but not the M state, may interact with the caps (poles) in the
623 spherocylinders, with an extra interaction again represented by a square well, with range 1
624 and strength ϵ_C. This interaction simulates binding between dimeric MinD and MinJ. Various
625 cases were considered but results are reported, for simplicity for two cases only: ϵ_C=0 (no
626 additional polar interaction), or ϵ_C = 0.7 ϵ_M . A third parameter which varies between M and
627 D is the diffusion coefficient: for simplicity, unless otherwise stated, we assume this to scale
628 inversely with molecular weight, so that the diffusivity of the dimer, D_d, is half that of the
629 monomer, D_m.

630 Key to the formation of the gradient is the fact that the reaction between the M and
631 D states of MinD is not in thermodynamic equilibrium, as it is linked to ATP hydrolysis. In our
632 model, D turns into M, due to ATP hydrolysis, at a constant rate k_{ATP}, in all cases. We
633 consider instead three cases for the dimerization reaction. In our baseline model the
634 conversion of M into D also occurred at the same rate in the cytoplasm, at the membrane
635 and at the pole. We have set this rate such that the M and D state are on average
636 comparable in steady state, as suggested by our experiments. We also considered the case
637 where dimerization at the membrane occurs 2-fold more often at the membrane, and a
638 third case where polar localization (through MinJ interaction) strongly stimulates
639 dimerization, so that the M to D transition occurs at a rate $k_{pole} >> k_{ATP}$ at poles. When
640 considering polar stimulation, dimerization occurs at a rate $k_{ATP}/10$ in the cytosol; otherwise,
641 rates of dimerization and monomerization in the cytoplasm are equal. The diffusion of
642 monomeric MinD was set to 0.0033 in simulation units (corresponding to approximately 2
643 micron square per second, see below), where the hydrolysis rate k_{ATP} was set to 10^{-5}
644 (corresponding to 1/s, which is of the same order as used in previous modeling studies (5)).
645 When considering polar stimulation, we set k_{pole} such that dimerization at the pole occurs

646 with unit probability during a timestep (we have verified though that the results are
647 qualitatively similar down to at least a value of k_{pole} equal to 100 k_{ATP}). More details on the
648 parameters used in the model are given in the caption of Fig. 8, and Table S1.

649 To simulate the monomer (K16A) and dimer (D40A) mutants, we used another
650 version of the same model, in which all particles were of type M or D respectively, and the
651 rate of interconversion between the two was set to 0.

652 Simulation units may be mapped to physical units by noting that 1 space and time
653 units in simulations can be made to correspond to 0.08 microns and 10 microseconds,
654 respectively. Simulations were run typically for 10^7 time steps. Snapshots shown are for
655 systems which have reached equilibrium, so representing steady-state behaviour.

656

REFERENCES

ACKNOWLEDGEMENTS

We would like to thank especially Norbert Vischer for analysis and quantification of fluorescence images and developing ObjectJ plugins, members of the Bacterial Cell Biology group (University of Amsterdam) for insightful discussions, Dirk-Jan Scheffers for critical reading of the manuscript, and Marc Bramkamp for prior communications. This research was funded by EU Marie Curie ITN grants ATP-BCT (020496-2) and AMBER (317338), Marie Curie CIG grant DIVANTI (618452) and STW Vici grant (12128).

668 **REFERENCES**
669

670 1. Ramm B, Heermann T, Schwille P. 2019. The *E. coli* MinCDE system in the regulation
671 of protein patterns and gradients. Cell Mol Life Sci 76:4245-4273.
672 2. Kumar M, Mommer MS, Sourjik V. 2010. Mobility of cytoplasmic, membrane, and
673 DNA-binding proteins in *Escherichia coli*. Biophys J 98:552-9.
674 3. Howard M, Rutenberg AD, de Vet S. 2001. Dynamic compartmentalization of
675 bacteria: accurate division in *E. coli*. Phys Rev Lett 87:278102.
676 4. Meinhardt H, de Boer PA. 2001. Pattern formation in *Escherichia coli*: a model for the
677 pole-to-pole oscillations of Min proteins and the localization of the division site. Proc
678 Natl Acad Sci U S A 98:14202-7.
679 5. Huang KC, Meir Y, Wingreen NS. 2003. Dynamic structures in *Escherichia coli*:
680 spontaneous formation of MinE rings and MinD polar zones. Proc Natl Acad Sci U S A
681 100:12724-8.
682 6. Hu Z, Lutkenhaus J. 1999. Topological regulation of cell division in *Escherichia coli*
683 involves rapid pole to pole oscillation of the division inhibitor MinC under the control
684 of MinD and MinE. Mol Microbiol 34:82-90.
685 7. Raskin DM, de Boer PA. 1999. Rapid pole-to-pole oscillation of a protein required for
686 directing division to the middle of *Escherichia coli*. Proc Natl Acad Sci USA 96:4971-6.
687 8. Loose M, Fischer-Friedrich E, Ries J, Kruse K, Schwille P. 2008. Spatial regulators for
688 bacterial cell division self-organize into surface waves in vitro. Science 320:789-92.
689 9. Kruse K. 2002. A dynamic model for determining the middle of *Escherichia coli*.
690 Biophys J 82:618-27.
691 10. Di Ventura B, Sourjik V. 2011. Self-organized partitioning of dynamically localized
692 proteins in bacterial cell division. Mol Syst Biol 7:457.
693 11. Wurthner L, Brauns F, Pawlik G, Halatek J, Kerssemakers J, Dekker C, Frey E. 2022.
694 Bridging scales in a multiscale pattern-forming system. Proc Natl Acad Sci U S A
695 119:e2206888119.
696 12. Glock P, Brauns F, Halatek J, Frey E, Schwille P. 2019. Design of biochemical pattern
697 forming systems from minimal motifs. Elife 8.
698 13. Marston AL, Thomaides HB, Edwards DH, Sharpe ME, Errington J. 1998. Polar
699 localization of the MinD protein of *Bacillus subtilis* and its role in selection of the
700 mid-cell division site. Genes Dev 12:3419-30.
701 14. Marston AL, Errington J. 1999. Selection of the midcell division site in *Bacillus subtilis*
702 through MinD-dependent polar localization and activation of MinC. Mol Microbiol
703 33:84-96.
704 15. Gregory JA, Becker EC, Pogliano K. 2008. *Bacillus subtilis* MinC destabilizes FtsZ-rings
705 at new cell poles and contributes to the timing of cell division. Genes Dev 22:3475-
706 88.
707 16. Levin PA, Shim JJ, Grossman AD. 1998. Effect of minCD on FtsZ ring position and
708 polar septation in *Bacillus subtilis*. J Bacteriol 180:6048-51.
709 17. Bi E, Lutkenhaus J. 1993. Cell division inhibitors SulA and MinCD prevent formation
710 of the FtsZ ring. J Bacteriol 175:1118-25.
711 18. de Boer PA, Crossley RE, Rothfield LI. 1989. A division inhibitor and a topological
712 specificity factor coded for by the minicell locus determine proper placement of the
713 division septum in *E. coli*. Cell 56:641-9.

714 19. de Boer PA, Crossley RE, Hand AR, Rothfield LI. 1991. The MinD protein is a
715 membrane ATPase required for the correct placement of the *Escherichia coli* division
716 site. EMBO J 10:4371-80.
717 20. Hu Z, Lutkenhaus J. 2000. Analysis of MinC reveals two independent domains
718 involved in interaction with MinD and FtsZ. J Bacteriol 182:3965-71.
719 21. Cordell SC, Anderson RE, Lowe J. 2001. Crystal structure of the bacterial cell division
720 inhibitor MinC. EMBO J 20:2454-61.
721 22. Park KT, Wu W, Lovell S, Lutkenhaus J. 2012. Mechanism of the asymmetric
722 activation of the MinD ATPase by MinE. Mol Microbiol 85:271-81.
723 23. Hu Z, Lutkenhaus J. 2003. A conserved sequence at the C-terminus of MinD is
724 required for binding to the membrane and targeting MinC to the septum. Mol
725 Microbiol 47:345-55.
726 24. Szeto TH, Rowland SL, Habrukowich CL, King GF. 2003. The MinD membrane
727 targeting sequence is a transplantable lipid-binding helix. J Biol Chem 278:40050-6.
728 25. Hu Z, Saez C, Lutkenhaus J. 2003. Recruitment of MinC, an inhibitor of Z-ring
729 formation, to the membrane in *Escherichia coli*: role of MinD and MinE. J Bacteriol
730 185:196-203.
731 26. de Boer PA, Crossley RE, Rothfield LI. 1992. Roles of MinC and MinD in the site-
732 specific septation block mediated by the MinCDE system of *Escherichia coli*. J
733 Bacteriol 174:63-70.
734 27. Park KT, Villar MT, Artigues A, Lutkenhaus J. 2017. MinE conformational dynamics
735 regulate membrane binding, MinD interaction, and Min oscillation. Proc Natl Acad
736 Sci U S A 114:7497-7504.
737 28. Hu Z, Lutkenhaus J. 2001. Topological regulation of cell division in E. coli.
738 spatiotemporal oscillation of MinD requires stimulation of its ATPase by MinE and
739 phospholipid. Mol Cell 7:1337-43.
740 29. Hu Z, Gogol EP, Lutkenhaus J. 2002. Dynamic assembly of MinD on phospholipid
741 vesicles regulated by ATP and MinE. Proc Natl Acad Sci USA 99:6761-6.
742 30. Lackner LL, Raskin DM, de Boer PA. 2003. ATP-dependent interactions between
743 *Escherichia coli* Min proteins and the phospholipid membrane *in vitro*. J Bacteriol
744 185:735-49.
745 31. Rowlett VW, Margolin W. 2013. The bacterial Min system. Curr Biol 23:R553-6.
746 32. Bramkamp M, Emmins R, Weston L, Donovan C, Daniel RA, Errington J. 2008. A novel
747 component of the division-site selection system of *Bacillus subtilis* and a new mode
748 of action for the division inhibitor MinCD. Mol Microbiol 70:1556-69.
749 33. Patrick JE, Kearns DB. 2008. MinJ (YvjD) is a topological determinant of cell division in
750 *Bacillus subtilis*. Mol Microbiol 70:1166-79.
751 34. Lenarcic R, Halbedel S, Visser L, Shaw M, Wu LJ, Errington J, Marenduzzo D, Hamoen
752 LW. 2009. Localisation of DivIVA by targeting to negatively curved membranes.
753 EMBO J 28:2272-2282.
754 35. Ramamurthi KS, Losick R. 2009. Negative membrane curvature as a cue for
755 subcellular localization of a bacterial protein. Proc Natl Acad Sci USA 106:13541-5.
756 36. Howard M. 2004. A mechanism for polar protein localization in bacteria. J Mol Biol
757 335:655-63.
758 37. Feddersen H, Wurthner L, Frey E, Bramkamp M. 2021. Dynamics of the *Bacillus*
759 *subtilis* Min System. mBio 12:e00296-21.

760 38. Karoui ME, Errington J. 2001. Isolation and characterization of topological specificity
761 mutants of minD in Bacillus subtilis. Mol Microbiol 42:1211-21.
762 39. Hayashi I, Oyama T, Morikawa K. 2001. Structural and functional studies of MinD
763 ATPase: implications for the molecular recognition of the bacterial cell division
764 apparatus. EMBO J 20:1819-28.
765 40. Wu W, Park KT, Holyoak T, Lutkenhaus J. 2011. Determination of the structure of the
766 MinD-ATP complex reveals the orientation of MinD on the membrane and the
767 relative location of the binding sites for MinE and MinC. Mol Microbiol 79:1515-28.
768 41. Story RM, Steitz TA. 1992. Structure of the recA protein-ADP complex. Nature
769 355:374-6.
770 42. Leonard TA, Butler PJ, Lowe J. 2005. Bacterial chromosome segregation: structure
771 and DNA binding of the Soj dimer - a conserved biological switch. EMBO J 24:270-82.
772 43. Landgraf D, Okumus B, Chien P, Baker TA, Paulsson J. 2012. Segregation of molecules
773 at cell division reveals native protein localization. Nat Methods 9:480-2.
774 44. Lewis PJ, Marston AL. 1999. GFP vectors for controlled expression and dual labelling
775 of protein fusions in *Bacillus subtilis*. Gene 227:101-10.
776 45. Ghosal D, Trambaiolo D, Amos LA, Lowe J. 2014. MinCD cell division proteins form
777 alternating copolymeric cytomotive filaments. Nat Commun 5:5341.
778 46. Conti J, Viola MG, Camberg JL. 2015. The bacterial cell division regulators MinD and
779 MinC form polymers in the presence of nucleotide. FEBS Lett 589:201-6.
780 47. Huang H, Wang P, Bian L, Osawa M, Erickson HP, Chen Y. 2018. The cell division
781 protein MinD from *Pseudomonas aeruginosa* dominates the assembly of the MinC-
782 MinD copolymers. J Biol Chem 293:7786-7795.
783 48. Wang N, Zhang T, Du S, Zhou Y, Chen Y. 2022. How Do MinC-D Copolymers Act on Z-
784 Ring Localization Regulation? A New Model of *Bacillus subtilis* Min System. Front
785 Microbiol 13:841171.
786 49. Park KT, Du S, Lutkenhaus J. 2015. MinC/MinD copolymers are not required for Min
787 function. Mol Microbiol 98:895-909.
788 50. Strahl H, Hamoen LW. 2010. Membrane potential is important for bacterial cell
789 division. Proc Natl Acad Sci USA 107:12281-6.
790 51. Gouttenoire J, Montserret R, Kennel A, Penin F, Moradpour D. 2009. An amphipathic
791 alpha-helix at the C terminus of hepatitis C virus nonstructural protein 4B mediates
792 membrane association. J Virol 83:11378-84.
793 52. Adams DW, Wu LJ, Errington J. 2015. Nucleoid occlusion protein Noc recruits DNA to
794 the bacterial cell membrane. EMBO J 34:491-501.
795 53. Allen MP, Tildesley DJ. 1987. Computer simulations of liquids.
796 54. Binder K, Heermann DW. 2002. Monte Carlo Simulation in Statistical Physics: An
797 Introduction, 4th ed, vol 80.
798 55. Whitelam S, Geissler PL. 2007. Avoiding unphysical kinetic traps in Monte Carlo
799 simulations of strongly attractive particles. J Chem Phys 127:154101.
800 56. Sanz E, Marenduzzo D. 2010. Dynamic Monte Carlo versus Brownian dynamics: A
801 comparison for self-diffusion and crystallization in colloidal fluids. J Chem Phys
802 132:194102.
803 57. Feddersen H, Bramkamp M. 2024. Mechanistic Insights into MinD Regulation and
804 Pattern Formation in *Bacillus subtilis*. bioRxiv 20240708602513.

805 58. Suefuji K, Valluzzi R, RayChaudhuri D. 2002. Dynamic assembly of MinD into filament
806 bundles modulated by ATP, phospholipids, and MinE. Proc Natl Acad Sci U S A
807 99:16776-81.
808 59. Heermann T, Ramm B, Glaser S, Schwille P. 2020. Local Self-Enhancement of MinD
809 Membrane Binding in Min Protein Pattern Formation. J Mol Biol 432:3191-3204.
810 60. Mika JT, Thompson AJ, Dent MR, Brooks NJ, Michiels J, Hofkens J, Kuimova MK. 2016.
811 Measuring the Viscosity of the *Escherichia coli* Plasma Membrane Using Molecular
812 Rotors. Biophys J 111:1528-1540.
813 61. Mullineaux CW, Nenninger A, Ray N, Robinson C. 2006. Diffusion of green
814 fluorescent protein in three cell environments in *Escherichia coli*. J Bacteriol
815 188:3442-8.
816 62. Ptacin JL, Lee SF, Garner EC, Toro E, Eckart M, Comolli LR, Moerner WE, Shapiro L.
817 2010. A spindle-like apparatus guides bacterial chromosome segregation. Nat Cell
818 Biol 12:791-8.
819 63. Leipe DD, Wolf YI, Koonin EV, Aravind L. 2002. Classification and evolution of P-loop
820 GTPases and related ATPases. J Mol Biol 317:41-72.
821 64. Surovtsev IV, Lim HC, Jacobs-Wagner C. 2016. The Slow Mobility of the ParA
822 Partitioning Protein Underlies Its Steady-State Patterning in Caulobacter. Biophys J
823 110:2790-2799.
824 65. MacCready JS, Hakim P, Young EJ, Hu L, Liu J, Osteryoung KW, Vecchiarelli AG, Ducat
825 DC. 2018. Protein gradients on the nucleoid position the carbon-fixing organelles of
826 cyanobacteria. Elife 7.
827 66. Veiga H, Jousselin A, Schaper S, Saraiva BM, Marques LB, Reed P, Wilton J, Pereira
828 PM, Filipe SR, Pinho MG. 2023. Cell division protein FtsK coordinates bacterial
829 chromosome segregation and daughter cell separation in *Staphylococcus aureus*.
830 EMBO J doi:10.15252/embj.2022112140:e112140.
831 67. Deeng J, Chan KY, van der Sluis EO, Berninghausen O, Han W, Gumbart J, Schulten K,
832 Beatrix B, Beckmann R. 2016. Dynamic Behavior of Trigger Factor on the Ribosome. J
833 Mol Biol 428:3588-602.
834 68. Ishikawa K, Matsuoka S, Hara H, Matsumoto K. 2017. Septal membrane localization
835 by C-terminal amphipathic alpha-helices of MinD in *Bacillus subtilis* mutant cells
836 lacking MinJ or DivIVA. Genes Genet Syst 92:81-98.
837 69. Hamoen LW, Smits WK, de Jong A, Holsappel S, Kuipers OP. 2002. Improving the
838 predictive value of the competence transcription factor (ComK) binding site in
839 *Bacillus subtilis* using a genomic approach. Nucleic Acids Res 30:5517-28.
840 70. Morimoto T, Loh PC, Hirai T, Asai K, Kobayashi K, Moriya S, Ogasawara N. 2002. Six
841 GTP-binding proteins of the Era/Obg family are essential for cell growth in *Bacillus*
842 *subtilis*. Microbiology 148:3539-52.
843 71. Fort P, Errington J. 1985. Nucleotide sequence and complementation analysis of a
844 polycistronic sporulation operon, *spoVA*, in *Bacillus subtilis*. J Gen Microbiol
845 131:1091-105.
846 72. Syvertsson S, Wang B, Staal J, Gao Y, Kort R, Hamoen LW. 2021. Different Resource
847 Allocation in a *Bacillus subtilis* Population Displaying Bimodal Motility. J Bacteriol
848 203:e0003721.
849 73. Vischer NO, Verheul J, Postma M, van den Berg van Saparoea B, Galli E, Natale P,
850 Gerdes K, Luirink J, Vollmer W, Vicente M, den Blaauwen T. 2015. Cell age dependent

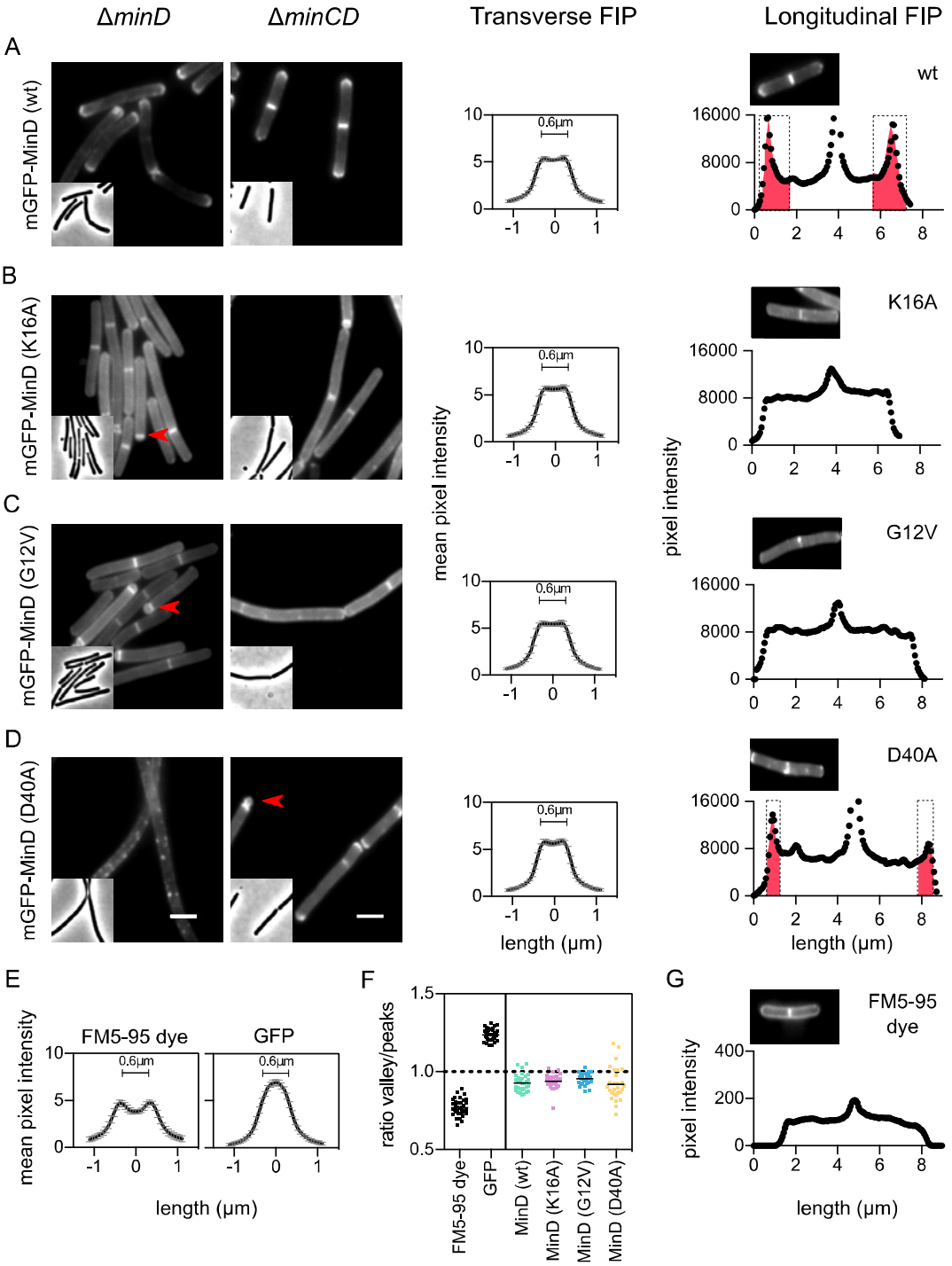

concentration of *Escherichia coli* divisome proteins analyzed with ImageJ and ObjectJ. Front Microbiol 6:586.

Fig. 1. Localization of monomeric and dimeric MinD variants

Cellular localization of (A) wild type MinD, (B) MinD K16A, (C) MinD G12V , and (D) MinD

857 D40A. Localization was monitored by an N-terminal mGFP fusion. Fusion proteins were
858 expressed in either a Δ*minD* or Δ*minCD* background. Fluorescence images (left panels) and
859 corresponding phase contrast images (inset) are shown in the left panels. Some minicells are
860 indicated with red arrows. Scale bar is 2 µm. Middle panels show the transverse
861 fluorescence intensity profiles (FIP) with standard deviations calculated using an average of
862 at least 30 cells (Δ*minCD* background) per data set. Right panels depict the longitudinal
863 fluorescence intensity profiles (FIP) using the Δ*minCD* background. The manually shaded red
864 areas highlight the polar gradients. Additional examples for wild type MinD and the D40A
865 variants are shown in Fig. S3. (E) Transversal fluorescence intensity profile (FIP) with
866 standard deviations of exponentially growing wild-type cells stained with fluorescence
867 membrane dye FM5-95, and wild-type cells expressing GFP are shown as controls. (F)
868 Membrane affinities, with median values, estimated from the valley/peak ratios shown in
869 the middle panels of (A-D) and controls (E). (G) Longitudinal fluorescence intensity profile
870 (FIP) along the exponentially growing wild-type cells stained with the fluorescence
871 membrane dye FM5-95. Strains used in (A): LB249 and LB305, (B): LB250 and LB306, (C):
872 LB251 and LB307, (D): LB252 and LB308, (E): LB609 and (G) 168.
873

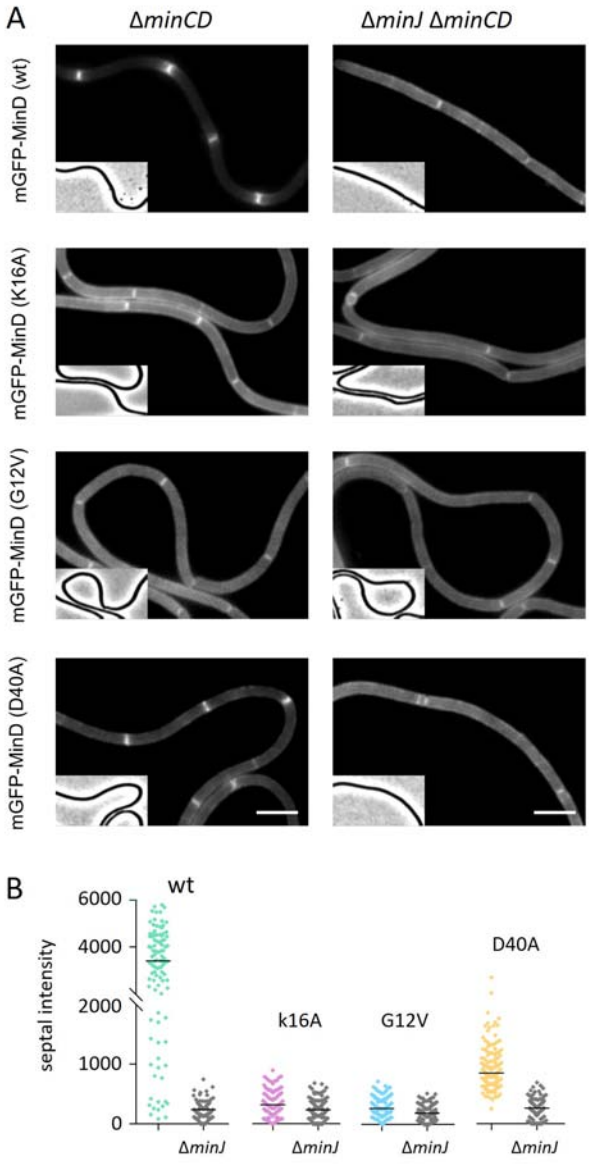

874

875

876 **Fig. 2. Effect of a *minJ* deletion on MinD-GFP localization**

877 (A) Fluorescence microscopy images of Δ*minCD* and Δ*minJ* Δ*minCD* mutant cells expressing

878 different mGFP–MinD variants. Corresponding phase contrast images are shown in the

879 insets. (B) Quantification of related septal fluorescence intensities, with median values, at

880 septa (n > 100). Since the strongly filamentous Δ*minJ* strain is delicate to handle, cells were

881 grown on agarose patches on microscopy slides. Scale bar is 5 µm. Strains used for wt:

882 LB405 and LB409, K16A: LB406 and LB410, G12V: LB407 and LB411, and D40A: LB408 and

883 LB412.

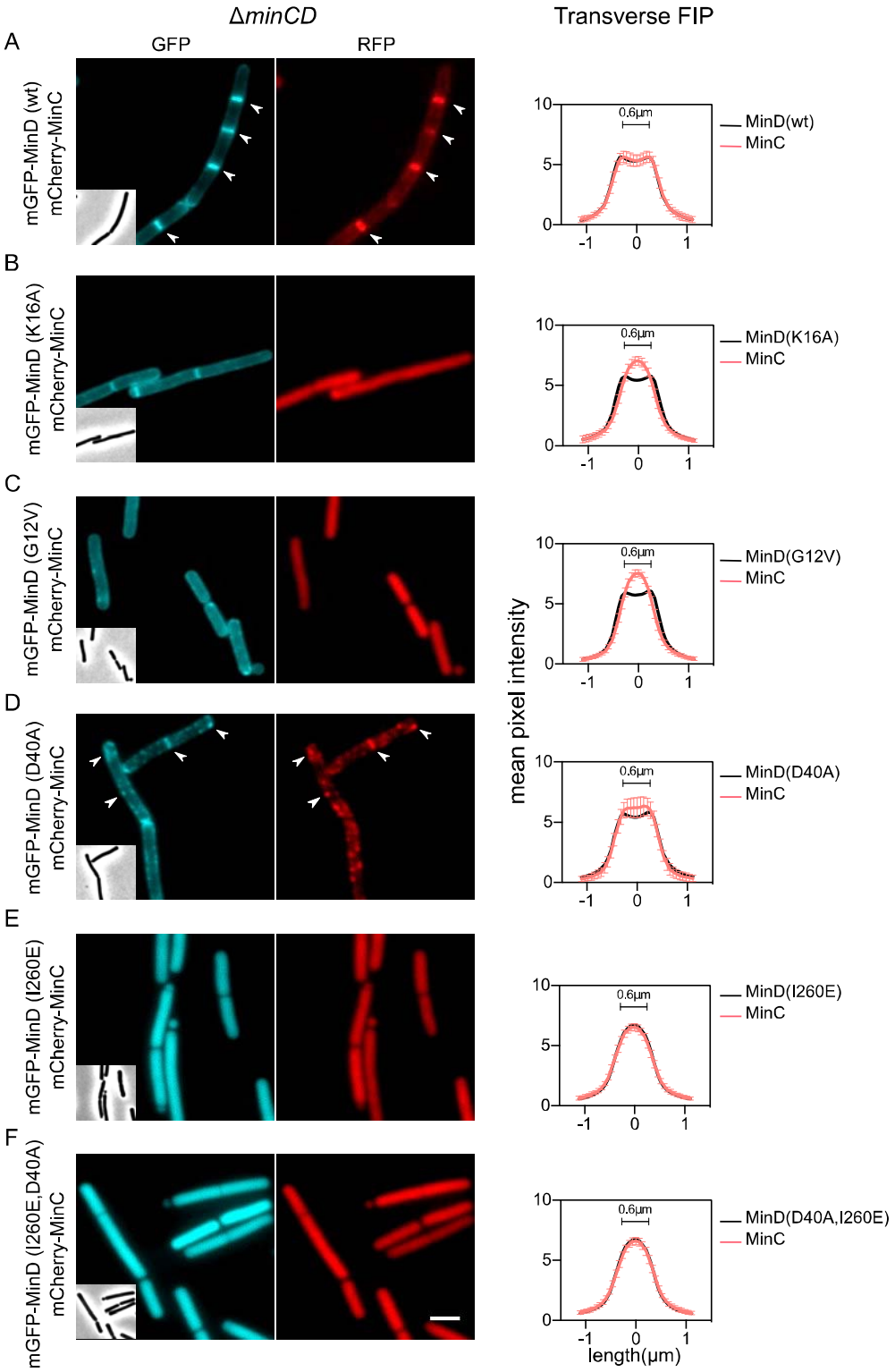

Fig. 3. Membrane recruitment of MinC by MinD variants

Fluorescence microscopy images of cells expressing different mGFP–MinD variants (cyan) and mCherry–MinC (red). Corresponding phase contrast images shown in the insets. (A)

888 Wild type MinD, (B) MinD K16A, (C) MinD G12V, (D) MinD D40A , (E) MinD I260E, (F) MinD
889 D40A, I260E. Right panels show the transverse fluorescence intensity profiles (FIP) with
890 standard deviations averaged over at least 30 cells. White arrows in (D) highlights
891 colocalization. Scale bar is 2 µm. mGFP–MinD variants and mCherry–MinC were expressed
892 in a Δ*minCD* background strain Strains used: (A) LB318, (B) LB319, (C) LB320, (D) LB321. (E)
893 LB643 and (F) LB644.

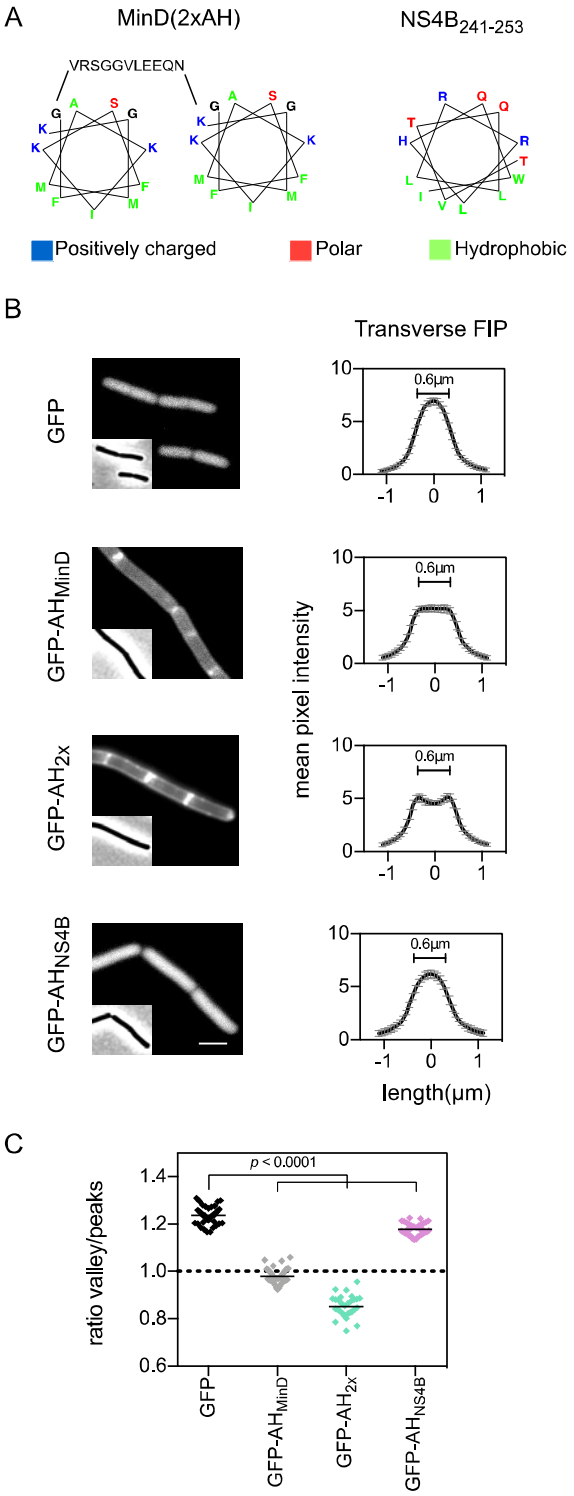

894

895 **Fig. 4. Membrane association of different amphipathic helices**

896 (A) Schematic presentation of the tandem amphipathic helix and the weak amphipathic

897 helix from Hepatitis C virus protein $NS4B_{241-253}$. (B) Fluorescence microscopy images and

898 transverse fluorescence intensity profiles (FIP) with standard deviations of cells expressing

899 the different amphipathic helix sequences fused to the C-terminus of GFP. A strain
900 expressing cytoplasmic GFP was included for comparison. Scale bar is 2 µm. Strains used:
901 FBB043 (GFP-AH_{MinD}), FBB05 (GFP-AH_{2x}), FBB046 (GFP-AH_{NS4B}), LB609 (GFP). (C) Average
902 membrane affinities calculated from the transverse fluorescence intensity profiles (n > 30).
903 Significance of difference was confirmed using t-test.

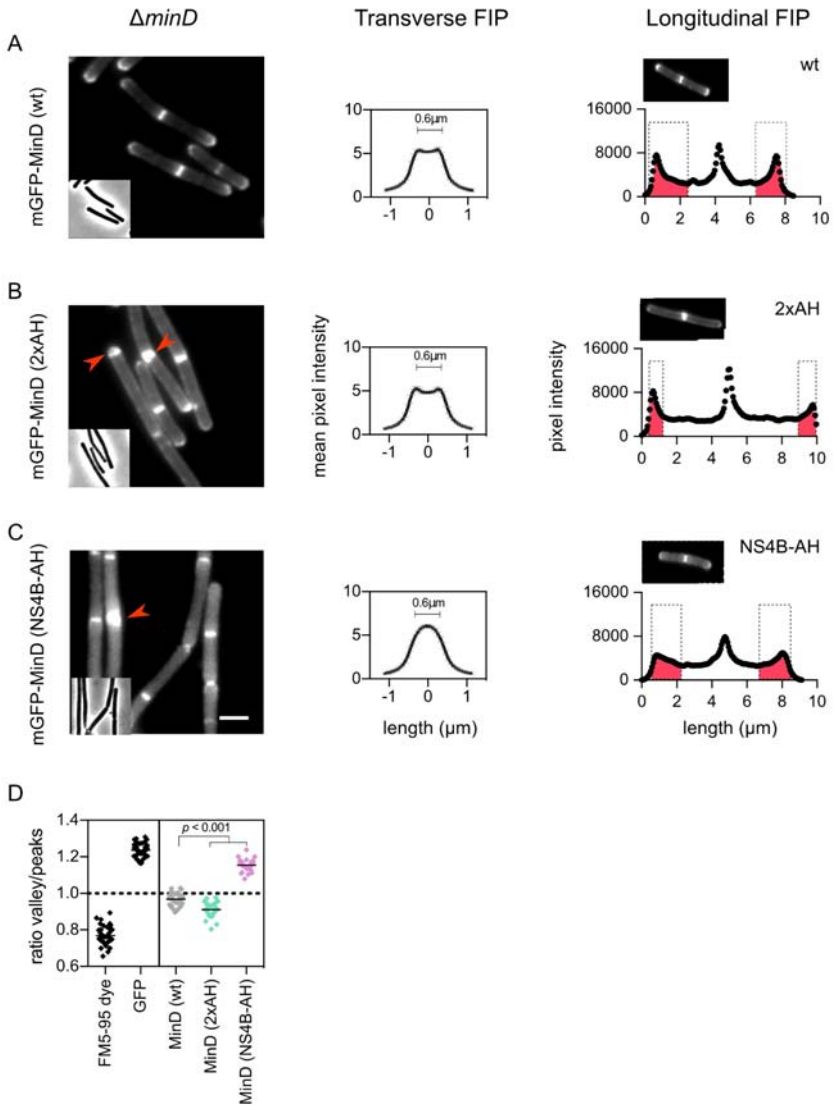

904

905 **Fig. 5. Membrane affinity affects MinD gradient**

906 Fluorescence microscopy and fluorescence intensity profiles (FIP) with standard deviations
907 of cells expressing mGFP-MinD containing either the native amphipathic helix (wt) (A), the
908 tandem MinD amphipathic helix (2xAH) (B) or the weak Hepatitis C virus protein NS4B
909 amphipathic helix (NS4B-AH) (C). The manually shaded red areas highlight the polar
910 gradients. Additional examples are shown in Fig. S4. (D) Relative membrane affinities with
911 median values of the different mGFP-MinD variants calculated from transverse fluorescence
912 intensity profiles (n > 30). Significance of difference was confirmed using t-test. The MinD
913 variants were expressed in a Δ*minD* background. Phase contrast images are shown as insets.
914 Some double septa are indicated with red arrows. Scale bar is 2 µm. Red areas in the
915 intensity profiles highlight the polar gradients. Strains used in (A) LB249, in (B) LB507, in (C)

916 LB508.

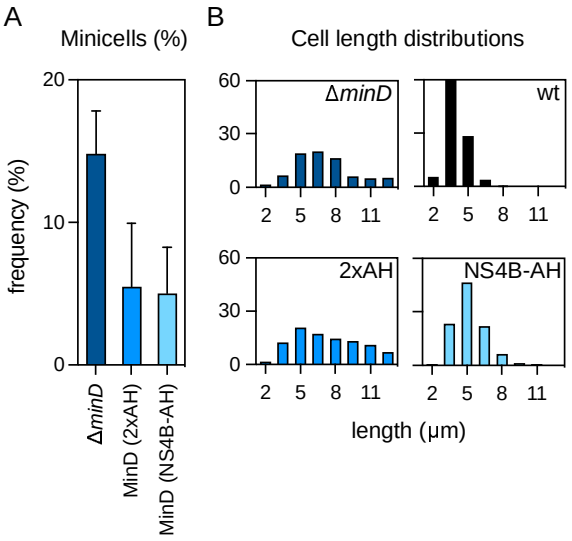

Fig. 6. Functionality of MinD with different membrane affinities

(A) Minicell formation in cells expressing mGFP-MinD with different membrane affinities. The MinD variants were expressed in a Δ*minD* background (*n* > 300). Standard deviations are indicated. (B) Cell length distributions of the different strains (*n* > 300). Strains used: 1901 (Δ*minD*), LB249 (wild type MinD), LB507 (2xAH) and LB508 (NS4B-AH).

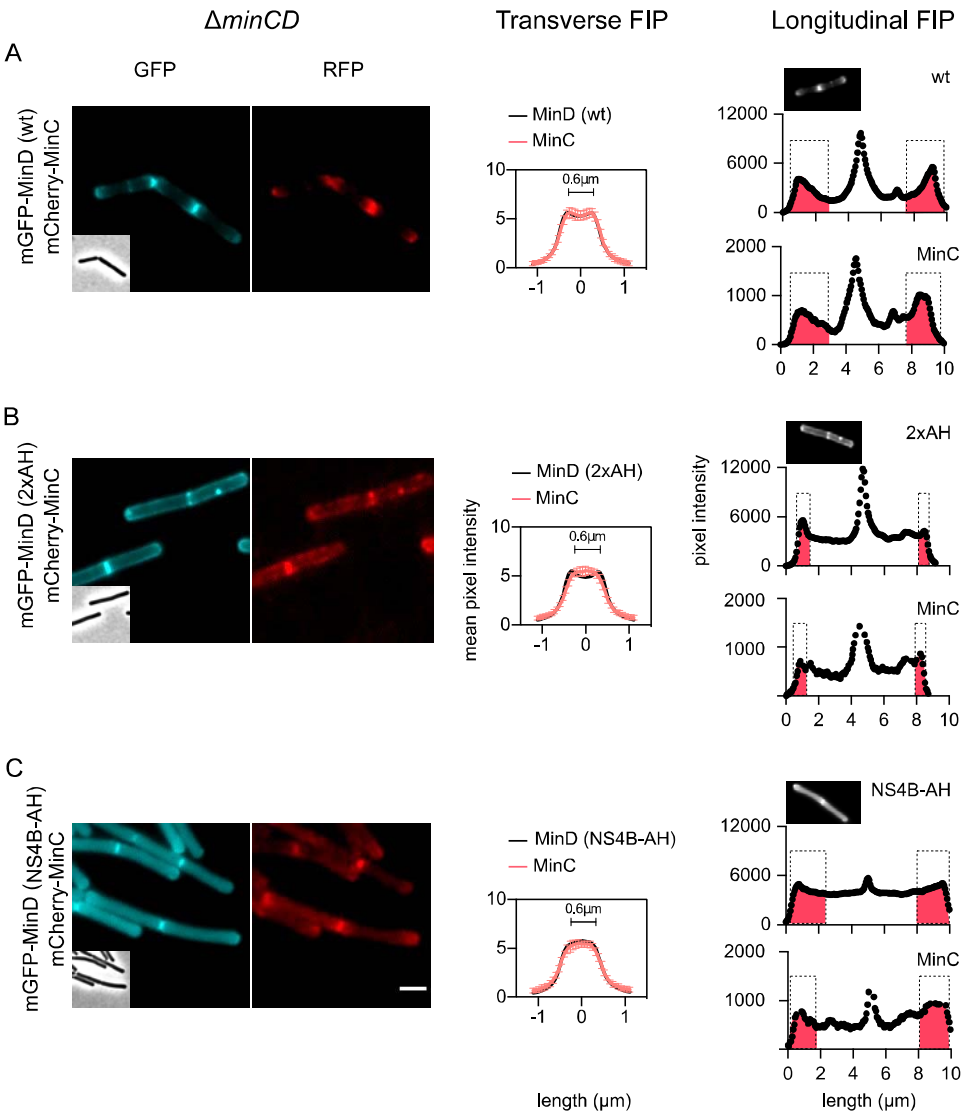

Fig. 7. Increased MinD membrane affinity affects MinC recruitment

Fluorescence microscopy images of cells expressing mGFP-MinD (cyan) and mCherry-MinC (red), with either the native membrane anchor (A), the tandem amphipathic helix (B), or the weak Hepatitis C virus protein NS4B derived amphipathic helix (C). Corresponding phase contrast images are shown in insets. Scale bar is 2 µm. Transverse fluorescence intensity profiles (FIP) with standard deviations are shown in the right panels (n > 30). Right panels depict the longitudinal fluorescence intensity profiles (FIP) with manually shaded red areas to highlight the polar gradients. Additional examples are shown in Fig. S6. The mGFP-MinD variants and mCherry-MinC were expressed in a Δ*minCD* background strain. Strains used: (A) LB318, (B) LB584, (C) LB559.

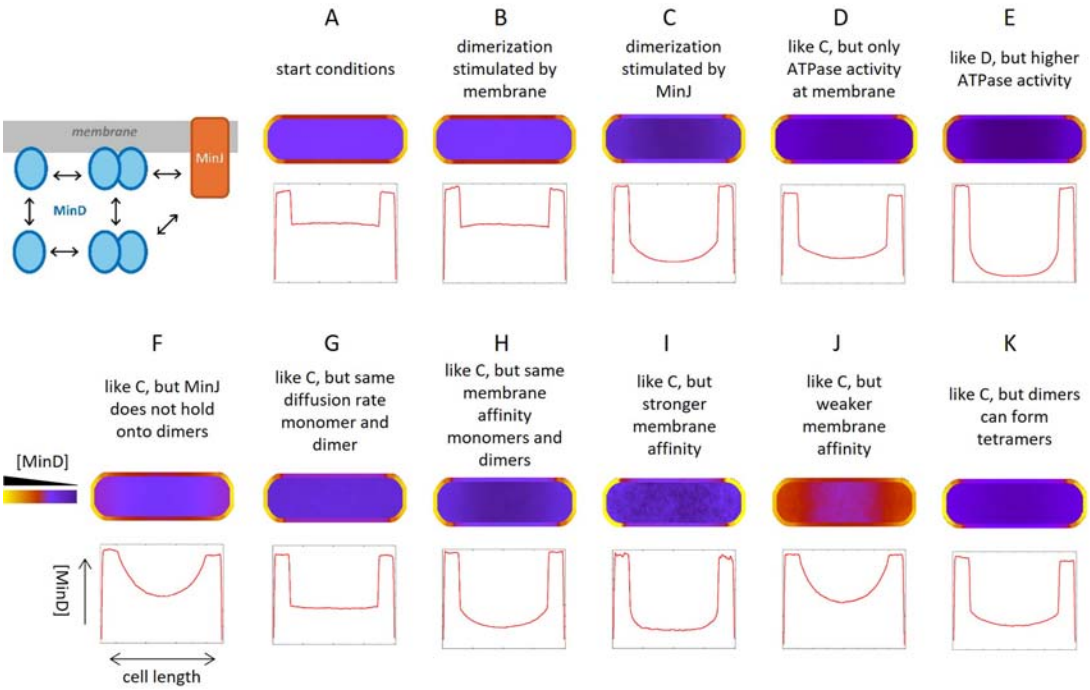

Fig. 8. Kinetic Monte Carlo simulations of MinD localization

Whole-cell kinetic Monte-Carlo simulations of MinD distribution, taking into account dimer-to-monomer transition rates (ATPase activity), membrane affinities, and MinJ interaction (schematic model). The following conditions have been simulated: (A) Start situation whereby (i) diffusion along the membrane is 10-fold slower compared to cytoplasm, (ii) MinD dimer diffuses 2-fold slower compared to the monomer in both environments, (iii) 10 % stronger membrane affinity for dimer, (iv) membrane dwell time of monomers and dimers on average 1.4-4.5 sec, (v) dimerization and monomerization rates such that dimers and monomers are approximately in a 1:1 ratio, (vi) transition from dimer to monomer occurs stochastically with a half-life of approximately 1/sec, and (vii) MinD dimers in close proximity of polar regions (peak MinJ concentration) will remain attached for some time, so that approximately 25 % of MinD dimers is associated with the polar caps, representing MinJ. (B) Same as simulation A, but membrane attached monomers have a 2-fold higher chance of forming dimers compared to cytoplasmic monomers. (C) Same as simulation A, but MinJ also stimulates MinD dimerization. (D) Same as simulation C, but MinD ATPase activity, i.e. dimer-to-monomer transition, only occurs at the membrane. (E) Same as

954 simulation D, but with a 10-fold higher ATPase activity, i.e. dimer-to-monomer transition. (F)
955 Same as simulation C. but MinD dimers are not retained by MinJ. (G) Same as simulation C.
956 but diffusion rates of monomer and dimer are the same. (H) Same as simulation C. but the
957 membrane affinity of MinD monomers and dimers is the same. (I) Same as simulation C. but
958 membrane affinity of MinD is stronger, such that the diffusion is a further 10-fold slower on
959 the membrane. (J) Same as simulation C, but membrane affinity of MinD is 2-fold weaker.
960 (K) Same as simulation C, but now MinD dimers can also form tetramers. Graphs indicate
961 the average lateral projection of MinD in simulated cells.